

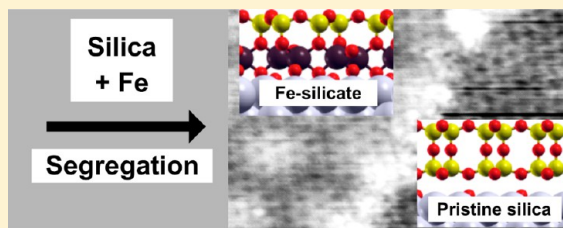
# Atomic Structure of an Ultrathin Fe-Silicate Film Grown on a Metal: A Monolayer of Clay?

Radosław Włodarczyk,<sup>†,§</sup> Joachim Sauer,<sup>\*,†</sup> Xin Yu,<sup>‡,§</sup> Jorge Anibal Boscoboinik,<sup>‡</sup> Bing Yang,<sup>‡</sup> Shamil Shaikhutdinov,<sup>\*,‡</sup> and Hans-Joachim Freund<sup>‡</sup>

<sup>†</sup>Institute of Chemistry, Humboldt-Universität zu Berlin, Unter den Linden 6, 10099 Berlin, Germany

<sup>‡</sup>Chemical Physics Department, Fritz-Haber-Institut der Max-Planck-Gesellschaft, Faradayweg 4-6, 14195 Berlin, Germany

**ABSTRACT:** Ultrathin Fe-doped silicate films were prepared on a Ru(0001) surface and, as a function of the Fe/Si ratio, structurally characterized by low-energy electron diffraction, X-ray photoelectron spectroscopy, infrared reflection–absorption spectroscopy, and scanning tunneling microscopy. Density functional theory (DFT) was used to identify the atomic structure. The results show that uniform substitution of Si by Fe in the silicate bilayer frame is thermodynamically unfavorable: the film segregates into a pure silicate and an Fe-silicate phase. The DFT calculations reveal that the Fe-silicate film with an Fe/Si = 1:1 ratio consists of a monolayer of  $[\text{SiO}_4]$  tetrahedra on top of an iron oxide monolayer. As such, it closely resembles the structure of the clay mineral nontronite, a representative of the Fe-rich smectites. Furthermore, the DFT calculations predict formation of bridging Fe–O–Ru bonds between the Fe-silicate film and the Ru substrate accompanied by charge transfer from the metal substrate to the film, so that iron is in the oxidation state +III as in nontronite.



## 1. INTRODUCTION

Recent progress in the preparation of well-defined ultrathin silicate and aluminosilicate films on metal single-crystal supports opened new possibilities for experimental and theoretical model studies on zeolites, aimed at a fundamental understanding of structure–reactivity relationships in these very complex materials.<sup>1</sup> It is established now that a silicate film can be grown either as a monolayer or as a bilayer of corner-sharing  $[\text{SiO}_4]$  tetrahedra.<sup>2</sup> Some of the  $\text{Si}^{4+}$  ions in the films can be substituted by  $\text{Al}^{3+}$ , thus resulting in an aluminosilicate film, which expose strongly acidic OH species like in catalytically active zeolites.<sup>3</sup> Following this approach, one could, in principle, prepare other zeolitic films, which would contain transition metal cations, as well. Metal-containing zeolites are commonly used as catalysts. For example, Fe-zeolites and Fe-silicates efficiently catalyze several industrially important oxidation reactions.<sup>4</sup> These materials are formed by substitution of a small fraction of  $\text{Si}^{4+}$  with  $\text{Fe}^{3+}$  in the framework. However, the nature of active species in these materials remains controversial owing to a huge variety of different Fe coordinations inside and out of the crystalline framework (see recent review 4b). It was suggested that at very low Fe concentrations the active species are isolated, coordinatively unsaturated  $\text{Fe}^{2+}$  ions grafted to the crystalline matrix.

The structural motif of well-ordered ultrathin silica films on metals basically resembles silica sheets like in phyllosilicates, for instance, micas. The two-dimensional sheets are characteristic of the crystal structures of clay minerals: they form alternating tetrahedral silicate (all Si) sheets and octahedral hydroxide (commonly, Al) sheets. Clay minerals often contain redox-

active  $\text{Fe}^{3+}$  species in the octahedral sheet, which participate in electron transfer reactions and play an important role in biogeochemical processes (see ref 5 and references therein).

Here, we make use of the new experimental possibilities to study metal substitution in a particular form of silicate structures using the same approach as previously applied for fabricating aluminosilicate films.<sup>3</sup> In this study, we report on the preparation of a well-ordered Fe-silicate thin film on a Ru(0001) substrate. Structural characterization was performed by low-energy electron diffraction (LEED), X-ray photoelectron spectroscopy (XPS), infrared reflection–absorption spectroscopy (IRAS), and scanning tunneling microscopy (STM) as a function of the Fe/Si ratio. Density functional theory (DFT) has been used to analyze the substitution patterns of Fe in the silicate film and its vibrational and electronic properties. The DFT results showed that, contrary to the Al distribution in aluminosilicates, which is governed by the avoidance of Al–O–Al pairs (Loewenstein's rule<sup>6</sup>), the Fe-silicate film consists of silica and iron oxide monolayer sheets (Fe/Si = 1:1). As such, it represents, in essence, a monolayer of nontronite, an Fe-rich smectite. The resulting films can further be used as suitable model systems for studying structure–property relationships in clay minerals.

## 2. METHODS AND MATERIALS

**2.1. Experiments.** The experiments were carried out in an ultrahigh vacuum (UHV) chamber equipped with LEED (from Omicron), XPS with a Scienta SES 200 hemispherical analyzer, IRAS

Received: August 23, 2013

Published: December 10, 2013



(Bruker), and STM (Omicron). The Ru(0001) crystal (99.99%, from MaTeck) was mounted on an Omicron sample holder. The temperature was measured by a type K thermocouple spot-welded to the edge of the crystal.

The clean Ru(0001) surface was obtained by repeated cycles of Ar<sup>+</sup> sputtering and annealing to 1300 K in UHV. Then the surface was precovered with a 3O(2 × 2)-layer by exposing to 3 × 10<sup>−6</sup> mbar O<sub>2</sub> at 1200 K for 5 min and cooling to 500 K prior to pumping oxygen out. Silicon was vapor-deposited onto the O/Ru(0001) surface at ~100 K in 2 × 10<sup>−7</sup> mbar O<sub>2</sub>. For preparation of Fe-containing films, Fe was vapor-deposited immediately after Si deposition. Final oxidation was performed in 5 × 10<sup>−6</sup> mbar O<sub>2</sub> at ~1150 K.

The XPS spectra were referenced by setting the Au 4f<sub>7/2</sub> level to 84.0 eV measured on a clean gold foil. The absolute intensity of the Si 2p, O 1s, and Fe 2p signals was calibrated via the spectra of pure SiO<sub>2</sub><sup>2b</sup> and FeO(111)<sup>7</sup> films on Ru(0001) as references. For all films, the sum of the molar amounts of Si and Fe was equal to the amount of Si necessary to prepare the bilayer silica film. The IRA spectra were recorded using p-polarized light at 84° grazing angle of incidence (resolution 4 cm<sup>−1</sup>). STM images were obtained at room temperature using Pt–Ir tips.

**2.2. DFT Calculations.** The DFT calculations used the Vienna ab initio simulation package (VASP).<sup>8</sup> The Perdew–Burke–Ernzerhof (PBE)<sup>9</sup> exchange–correlation functional was employed. The electron–ion interactions were described by the projector augmented wave (PAW) method.<sup>10</sup> Only the valence electrons (i.e., 5s and 4d for Ru, 3s and 3p for Si, 2s and 2p for O, and 4s and 3d for Fe) were explicitly considered. A semiempirical dispersion correction was added to qualitatively account for the dispersion forces, which is known as PBE + D approach.<sup>11</sup> A 400 eV cutoff for the plane wave basis set and an 8 × 4 × 1 Monkhorst–Pack grid<sup>12</sup> for the integrations of the first Brillouin zone were used. The positions of nuclei were relaxed until the forces were smaller than 5 × 10<sup>−3</sup> eV Å<sup>−1</sup>. Calculations for structures containing at least one iron atom were performed using high starting magnetic moments to converge to the high-spin solution. Harmonic vibrational frequencies were calculated using a central finite difference method with 0.02 Å displacements of the atoms in each Cartesian direction. The intensities were obtained from the derivatives of the dipole moment component perpendicular to the surface. To compensate for systematic errors of DFT, the vibrational frequencies are scaled by a factor of 1.0341, derived from a comparison between experimental and calculated frequencies for α-quartz (see Supporting Information in ref 2b).

### 3. RESULTS AND DISCUSSION

**3.1. Experimental Results.** We begin with the IRAS results since the IR spectroscopy turned out to be the most sensitive to the principal structure of the films.<sup>2a</sup> To recall, the bilayer SiO<sub>2</sub> film is characterized by two very strong and sharp phonon bands (see the top spectrum in Figure 1). The peak at 1300 cm<sup>−1</sup> is assigned to in-phase asymmetric stretching vibrations of the Si–O–Si linkage between two layers, and the signal at 692 cm<sup>−1</sup> to symmetric Si–O–Si stretching vibrations of Si–O–Si bonds nearly parallel to the surface; both modes are schematically shown in the inset.

Figure 1 displays a series of IRA spectra with increasing Fe/Si ratios. For simplicity, we refer to a compositional stoichiometry of the films as Fe<sub>x</sub>Si<sub>1−x</sub>O<sub>2</sub>, where  $x = \text{Fe}/(\text{Fe} + \text{Si})$  as measured by XPS. Clearly, the 1300 and 692 cm<sup>−1</sup> bands gradually attenuate and ultimately disappear at  $x \sim 0.5$ , whereas a sharp and strong band at 1005 cm<sup>−1</sup> together with a weak band at 674 cm<sup>−1</sup> appears and gains intensity with increasing Fe content. Note that all observed bands do not shift. Such behavior is characteristic for a two-component system and therefore indicates spatial segregation into the Fe-containing and pure silica phases rather than uniform Fe distribution in the silica matrix. Accordingly, the Fe-silicate phase expands in area, while

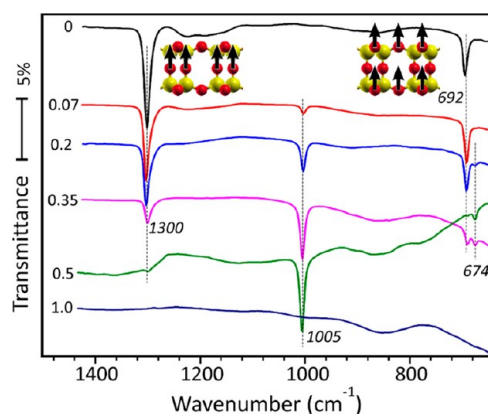


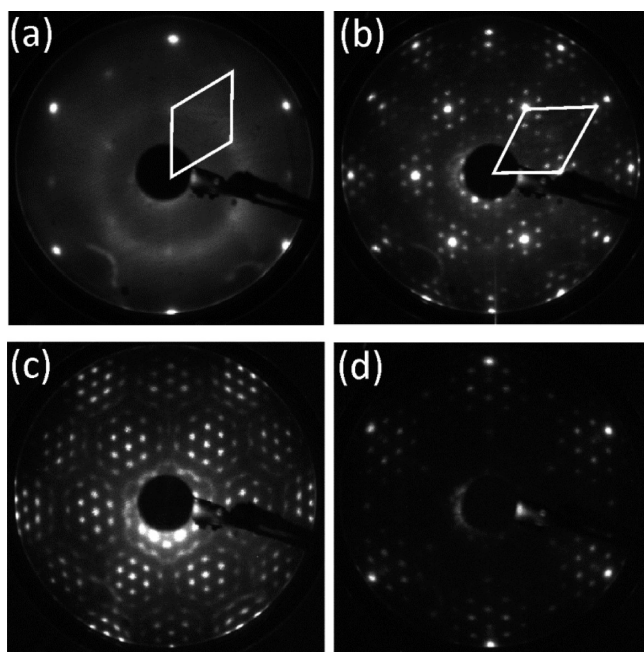
**Figure 1.** IRA spectra of Fe<sub>x</sub>Si<sub>1−x</sub>O<sub>2</sub> films on Ru(0001) as a function of the Fe content ( $x$ ) as indicated.

the pure silica phase shrinks at increasing Fe content. The observed spectral evolution is very different from that observed for aluminosilicate films, where Al incorporation only caused a red shift and broadening of the principal phonon bands (e.g., from 1300 to 1270 cm<sup>−1</sup>), although Al ions seem to exhibit some islanding at low Al/Si ratios as shown by STM.<sup>3</sup> Obviously, in the case of an Fe-silicate film, changes in the reduced masses of respective oscillators are much larger than in an Al-containing silicate film, and vibrational coupling of the two phases is hardly possible.

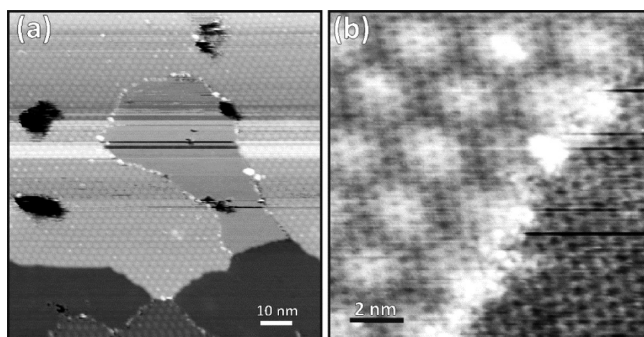
For comparison, we have also examined a “Si-free” film formed only by Fe deposition under the same preparation conditions, which ultimately resulted in an FeO(111) monolayer film.<sup>7</sup> This film has turned out to be IRAS-silent in the spectral region above 600 cm<sup>−1</sup> (see the bottom spectrum in Figure 1). This finding rules out the formation of the alone-standing FeO(111) structure in the resulting Fe-silicate films.

Figure 2 displays LEED patterns of the iron-silicate films. Interestingly, even small amounts of Fe in the films considerably improve ordering, as compared to the pure silicate films, which often show (2 × 2) diffraction spots together with a (2 × 2) ring characteristic for the vitreous silica (Figure 2a). The higher degree of crystallinity was previously observed also for Al-doped films, albeit maintaining the same (2 × 2) symmetry.<sup>3,13</sup> In contrast, in all Fe-containing films, the unit cell is rotated by 30° with respect to Ru(0001), and the lattice constant is shortened to about 5.25 Å (cf. 5.42 Å in the original film). Each integer spot is surrounded by satellite spots, which are characteristic for a Moiré structure commonly observed for epitaxial oxide layers, having a lattice mismatch to a metal support. As the Fe/Si ratio increases, the Moiré pattern dominates the surface. For comparison, Figure 2d shows the LEED pattern of an FeO(111)/Ru(0001) film. Although some similarities are obvious, the FeO(111)/Ru(0001) film shows an unrotated Ru(0001)-(8 × 8) structure, where eight Ru(0001) surface unit cells coincide with seven FeO(111) cells along the surface lattice directions.

The Moiré structure on Fe-silicate samples is clearly visible on STM images presented in Figure 3. The measured periodicity (~22 Å) agrees well with that measured by LEED (Figure 2). The surface area covered by the Moiré structure linearly increases with increasing Fe content, ultimately covering the entire surface at  $x \sim 0.5$ . Therefore, we may assign these areas to the Fe-silicate phase. The rest of the



**Figure 2.** LEED patterns (60 eV) of the  $\text{Fe}_x\text{Si}_{1-x}\text{O}_2$  films on Ru(0001) at  $x = 0$  (a), 0.2 (b), 0.5 (c), and 1 (d). The unit cells are indicated.



**Figure 3.** Large-scale (a) and high-resolution (b) STM images of the  $\text{Fe}_{0.2}\text{Si}_{0.8}\text{O}_2$  film. Tunneling conditions: sample bias 1.2 V and current 0.08 nA (a); 0.47 V and 0.08 nA (b).

surface shows a honeycomb-like structure with a  $\sim 5.5$  Å periodicity (see, for example, bottom right portion of Figure 3b) that is virtually identical to that observed on pure silicate films. The step height between terraces with identical structures is about 2.5 Å, which corresponds to a monatomic step on Ru(0001) underneath the oxide film. Within the same terrace, the Moiré surface is apparently higher than the pristine silica surface by 0.5–1 Å, depending on the tunneling conditions. In addition, the Fe-containing surface exhibits the honeycomb-like structure in the same orientation as the pure silicate phase in these films (see Figure 3b). Most likely, the STM contrast over Fe-containing areas reflects considerable changes in the electron density of states (only probed by STM) upon Fe incorporation. Therefore, solely geometrical considerations are hardly applicable here.

The same films were characterized by XPS. In all films, the binding energy (BE) of the Si 2p core level has the same value (102.6 eV) as in pure silicate films, where a Si atom is surrounded by four O atoms in  $[\text{SiO}_4]$  tetrahedra. The intensity of the Fe 2p signal (not shown here) scales with the Fe amounts, and the signal shape is very similar to that observed

for an FeO(111)/Ru(0001) film. Much larger differences are observed for the O 1s level. Figure 4 displays the spectra for

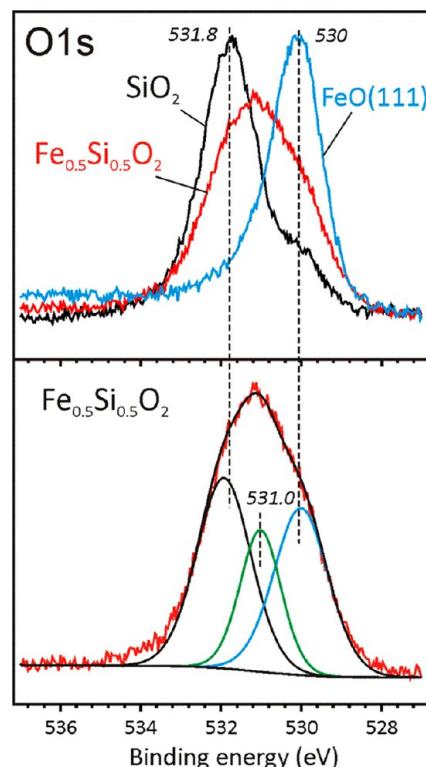


**Figure 4.** Top panel: XP spectra of the O 1s core level in pure  $\text{SiO}_2$ , FeO(111) and  $\text{Fe}_{0.5}\text{Si}_{0.5}\text{O}_2$  films on Ru(0001) as indicated. Bottom panel: Spectral deconvolution for the spectrum of the  $\text{Fe}_{0.5}\text{Si}_{0.5}\text{O}_2$  film.

pure  $\text{SiO}_2$  and FeO(111) films as well as for an  $\text{Fe}_{0.5}\text{Si}_{0.5}\text{O}_2$  film. The signal at 531.8 eV, which dominates for the silica films, is assigned to O bonded to Si. The additional signal observed in these films as a shoulder at  $\sim 530$  eV originates from the O atoms directly adsorbed onto the Ru surface in the “O-rich” structures.<sup>2b,14</sup> This signal almost coincides with the peak position on the FeO(111) film. With increasing Fe/Si ratio, the 531.8 eV peak attenuates, whereas the 530 eV signal gains intensity, thus forming a relatively broad O 1s signal, as shown in Figure 4 (top panel). Spectral deconvolution, however, revealed three oxygen species, which could tentatively be assigned to O atoms in Si–O–Si (532 eV), Si–O–Fe (531.0 eV), and Fe–O–Fe (530 eV) coordination environment (Figure 4, bottom panel).

Taken together, the experimental results show that at Fe/Si = 1 (i.e.,  $x = 0.5$ ) the surface is uniformly covered with a well-ordered film that is rotated by  $30^\circ$  with respect to Ru(0001) and shows the Moiré structure. In addition, STM and LEED results provide strong evidence that the honeycomb-like morphology persists for the Fe-silicate films, as well. The film shows a very characteristic, strong IRA band at  $1005\text{ cm}^{-1}$ . Obviously, the Si–O–Si linkage between layers is no longer present in this film. The formation of a monolayer silica film that directly adsorbs on Ru(0001) can also be excluded, as this would result in a band at  $\sim 1135\text{ cm}^{-1}$  associated with the Si–O–Ru linkages.<sup>2a</sup> On the basis of the reduced mass analysis, the band at  $1005\text{ cm}^{-1}$  could tentatively be associated with Si–O–Fe bonds.



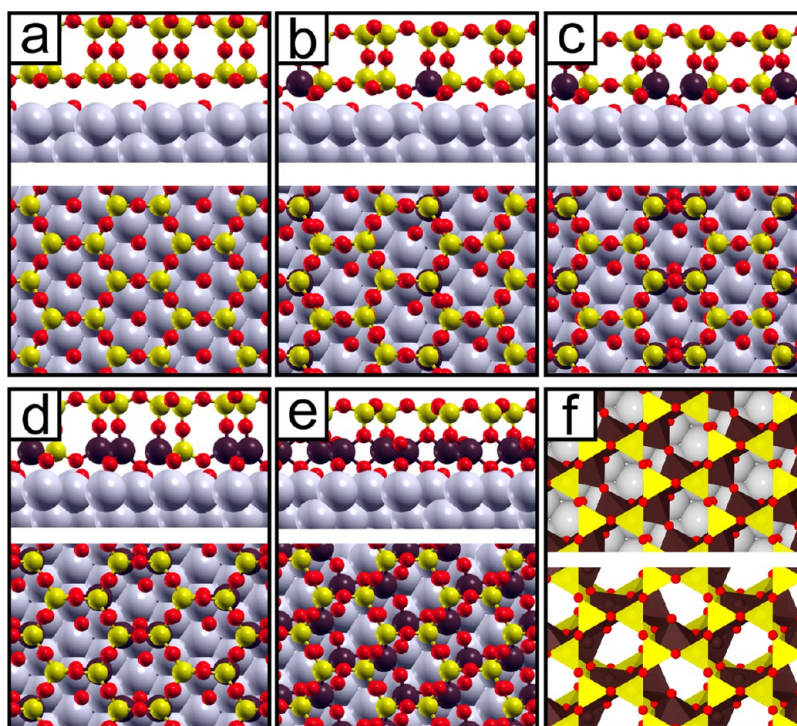


**Figure 5.** Top and side views of the most stable structures found by DFT at various Fe/Si ratios: (a)  $\text{Si}_8\text{O}_{16}\cdot 2\text{O}/\text{Ru}(0001)$ , (b)  $\text{FeSi}_7\text{O}_{16}\cdot 2\text{O}/\text{Ru}(0001)$ , (c)  $\text{Fe}_2\text{Si}_6\text{O}_{16}\cdot 2\text{O}/\text{Ru}(0001)$ , (d)  $\text{Fe}_3\text{Si}_5\text{O}_{16}\cdot 2\text{O}/\text{Ru}(0001)$ , (e)  $\text{Fe}_4\text{Si}_4\text{O}_{16}\cdot 2\text{O}/\text{Ru}(0001)$ . (f) Top views of  $\text{Fe}_4\text{Si}_4\text{O}_{16}\cdot 2\text{O}/\text{Ru}(0001)$  (top) and dehydroxylated nonttronite<sup>15</sup> (bottom) in polyhedral representation: Si, yellow; Fe, dark violet; O, red; Ru, gray.

As a starting point, one may consider a bilayer structure, where Fe replaces Al, like in the previously studied aluminosilicate films. Accordingly, the Fe ions could be placed either in the top or in the bottom layer, or both. A very uniform STM contrast observed in high-resolution images of Fe-containing areas indicates the preferential formation of only one structure rather than a mixture of several ones. The phase segregation into Fe-containing and pure silica, clearly observed by STM, is hardly consistent with the random distribution of Fe in the cation sublattice. Moreover, the latter scenario would contradict the XPS results showing substantial amounts of oxygen coordinated only to Fe, like in  $\text{FeO}(111)$  (see Figure 4). In fact, together with the measured Si/Fe = 1 ratio in a fully covered film, the O 1s XP spectra are consistent with the assumption that Fe ions substitute all Si in one, either the top or the bottom, layer. As the Fe–O bond in iron oxides ( $\sim 2.0$  Å) is much longer than the Si–O bond in silica ( $\sim 1.65$  Å), the Si substitution by Fe will be accompanied by severe lattice distortions, which could, however, be accommodated via interaction with the  $\text{Ru}(0001)$  support, which must be, in turn, much stronger than the van der Waals interaction in a pure silicate bilayer film. In addition, substituting Si with Fe in the top layer would result in the  $\text{Fe}^{4+}$  state, which is very unusual for iron oxides. In the case of aluminosilicate films, charge imbalance for  $\text{Al}^{3+}$  in the top layer was compensated by protons which formed bridging (Si–OH–Al) hydroxyls clearly identified by IRAS.<sup>3</sup> Water adsorption experiments on our Fe-silicate films did not result in any spectral features, which could be attributed to Si–OH–Fe species. It therefore appears that the Fe-containing layer is closer to the metal support than the Si layer. This would also be consistent with the STM results showing the same honeycomb-like surface structure as in a pure silicate film. However, the precise atomic structure of an Fe-

silicate film could not be determined solely on the basis of the experimental results presented above.

**3.2. DFT Results.** The previously studied<sup>14</sup> bilayer silica film with a  $\text{Si}_8\text{O}_{16}\cdot 2\text{O}/\text{Ru}(0001)$  composition in the  $(2 \times 2)$  unit cell (see Figure 5a) was used as a starting point for DFT modeling of the Fe-silicate film. Eight possible structures of  $\text{FeSi}_7\text{O}_{16}\cdot 2\text{O}/\text{Ru}(0001)$ , formed by Fe substitution of one of the eight Si atoms in the unit cell, were examined. The structures were optimized, and the most stable one is shown in Figure 5b. Consecutively, other substitutional  $\text{Fe}_n\text{Si}_{8-n}\text{O}_{16}\cdot 2\text{O}/\text{Ru}(0001)$  structures were created by iterative replacement of another Si atom in the most stable  $\text{Fe}_{n-1}\text{Si}_{8-(n-1)}\text{O}_{16}\cdot 2\text{O}/\text{Ru}(0001)$  structure and optimizing the atomic positions. The most stable structures for each ( $n = 2-4$ ) composition are shown in Figure 5.

Introducing one Fe atom does not affect the bilayer structure of the film, as shown in Figure 5b. The second Fe atom is preferably located as the nearest neighbor to the first Fe atom, and the bridging (Fe–O–Fe) oxygen atom shifts closer to the metal surface (Figure 5c). Also, for the third Fe atom, its position in the bottom layer is energetically preferable (Figure 5d). For the latter structure models, the Si–O–Fe and Si–O–Si linkages remain normal to the surface and the film maintains the structural motif of the bilayer silicate. Surprisingly, a qualitatively different structure was found for the most stable  $\text{Fe}_4\text{Si}_4\text{O}_{16}\cdot 2\text{O}/\text{Ru}(0001)$  system. It has turned out that the bilayer structure with four iron atoms in the bottom layer is not at the minimum on the potential energy surface. Instead, the structure rearranges to the one shown in Figure 5e. The topmost layer is virtually identical to the silica monolayer previously observed on  $\text{Ru}(0001)$ ,  $\text{Mo}(112)$ , and  $\text{SiC}(0001)$ ,<sup>1a,2a</sup> whereas the bottom layer is a two-dimensional network of edge-sharing and corner-sharing  $[\text{FeO}_5]$  square pyramids ordered in six-membered rings (four edge-sharing and

two corner-sharing connections). Furthermore, the six-membered rings of the Si- and of the Fe-containing layers are not aligned and slightly shifted with respect to each other.

Figure 6 shows the harmonic IRA spectra simulated for the  $\text{Fe}_n\text{Si}_{8-n}\text{O}_{16}\cdot 2\text{O}/\text{Ru}(0001)$  structures ( $n = 0-4$ ). Only modes

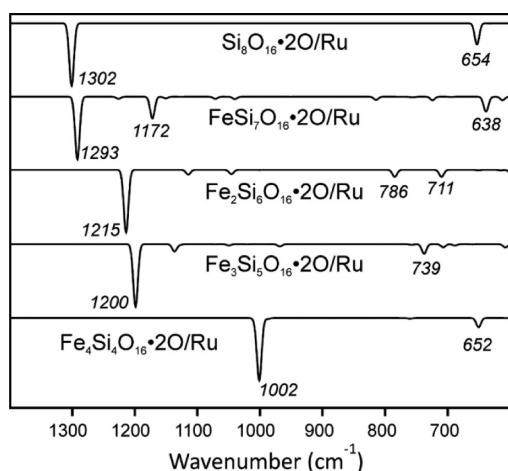
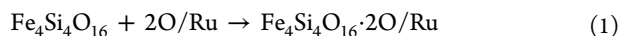


**Figure 6.** IRA spectra simulated for the structural models depicted in Figure 5. The spectra are scaled by a factor of 1.0341 (see Supporting Information in ref 2b).

above  $600\text{ cm}^{-1}$  will be discussed here to compare with the experimental results. Clearly, the number of IRA-active modes in the simulated spectra depends on the symmetry of the system. In the high-symmetry cases ( $n = 0$  and  $n = 4$ ), two principal bands are obtained, whereas the spectra of the lower symmetry structures ( $n = 1-3$ ) show many additional bands of much lower intensity. Those are associated with antiphase atom displacements, which are accompanied by small changes of the  $z$ -component of the net dipole moment. The high-frequency peaks originate from vibrations of the interlayer Si–O–Si (Si–O–Fe) linkages, whereas the low-frequency modes involve vibrations of the intralayer Si–O–Si (Si–O–Fe) bonds.

The spectrum for  $n = 4$  is considerably different from those obtained for  $n = 0-3$ . Iron atoms, constituting the bottom layer of the film (see Figure 5e), are not involved in the vibrations related to the most pronounced signal at  $1002\text{ cm}^{-1}$ , which is assigned solely to stretching of the Si–O bonds oriented perpendicular to the surface. The lower wavenumber band ( $652\text{ cm}^{-1}$ ) originates from the Si–O–Si bending. Such a large difference ( $\sim 300\text{ cm}^{-1}$ ) between the high wavenumber vibrations of the  $n = 0$  and  $n = 4$  structures ( $1302$  vs  $1002\text{ cm}^{-1}$ , respectively) indicates a complete change of the character of the silica layer. In the  $n = 0$  case, silica forms a bilayer, whereas for the  $n = 4$ , a monolayer is formed, and the spectrum resembles those observed for the monolayer silica films grown on Mo(112) and Ru(0001).<sup>1a</sup> The very good agreement between experimental and simulated IRA spectra validates the most stable structure shown in Figure 5e.

To get more insight into the nature of the interaction between the adlayer and the metal substrate in the  $\text{Fe}_4\text{Si}_4\text{O}_{16}\cdot 2\text{O}/\text{Ru}(0001)$  structure, Bader charges and work function were calculated, together with the adhesion energy for the reaction:



All structures occurring in this equation were optimized. The free  $\text{Fe}_4\text{Si}_4\text{O}_{16}$  adlayer is also an energy minimum structure,

which is found to be more stable than the free bilayer structure with isomorphous substitution of four Fe atoms. These properties as well as the  $\text{O}_{\text{surf}}\text{--Ru}$  bond distances are compared with the corresponding values obtained for the pristine silica bilayer  $\text{Si}_8\text{O}_{16}\cdot 2\text{O}/\text{Ru}(0001)$  in Table 1.

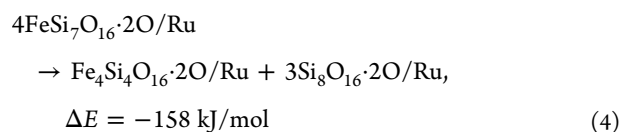
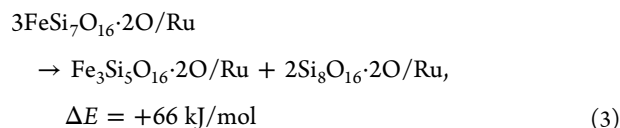
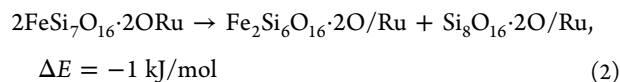
**Table 1.** Comparison of Selected Properties Calculated for the  $\text{Si}_8\text{O}_{16}\cdot 2\text{O}/\text{Ru}$  (Figure 5a) and  $\text{Fe}_4\text{Si}_4\text{O}_{16}\cdot 2\text{O}/\text{Ru}$  (Figure 5e) Films: Distance between Surface O Atoms and Ru Atoms,  $r(\text{O}_{\text{surf}}\text{--Ru})$ , Adhesion Energy Per Area,  $\Delta E_{\text{adh}}$  (eq 1), and Work Function Value Relative to the Pristine Silica Film,  $\Delta\Phi^a$

property	$\text{Si}_8\text{O}_{16}\cdot 2\text{O}_{\text{surf}}/\text{Ru}$	$\text{Fe}_4\text{Si}_4\text{O}_{16}\cdot 2\text{O}_{\text{surf}}/\text{Ru}$
$r(\text{O}_{\text{surf}}\text{--Ru})$ (pm)	202–203	201–203
$\Delta E_{\text{adh}}$ ( $\text{kJ}\cdot\text{mol}^{-1}\cdot\text{\AA}^{-2}$ )	−2.38 <sup>b</sup>	−15.48
adlayer Bader charge	−0.06	−1.54
$\Delta\Phi$ (eV)	0.0	1.4

<sup>a</sup>The values for the  $\text{Si}_8\text{O}_{16}\cdot 2\text{O}/\text{Ru}$  film are computed for the structure taken from ref 14. <sup>b</sup>From ref 2b.

For both structures, the oxygen atoms adsorbed directly at the metal surface,  $\text{O}_{\text{surf}}$ , are not involved in film–metal binding. The distances between  $\text{O}_{\text{surf}}$  and metal atoms,  $r(\text{O}_{\text{surf}}\text{--Ru})$ , fall in the region observed for the pure  $2\text{O}/\text{Ru}(0001)$  phase.<sup>16</sup> The pristine silica bilayer is only weakly bound to the metal by dispersion forces.<sup>2b</sup> For the Fe-silicate film, the calculated value of the adhesion energy per area,  $\Delta E_{\text{adh}}$ , is six times larger. The reason for this big difference is the formation of bridging Fe–O–Ru bonds. If the oxygen atoms are atop the Ru atoms ( $\text{O}^{\text{A}}$  in Figure 7c), short Ru–O bonds (195 pm) are formed, and when the oxygen atoms are at the hollow sites ( $\text{O}^{\text{B}}$  in Figure 7c), two longer bonds to the Ru surface atoms are formed (208 and 218 pm). The formation of these bonds with the Ru substrate is accompanied by charge transfer from the metal to the adlayer, as shown by the Bader charges, indicating that the metal becomes partially oxidized. This should result in an increase of the work function of the metal substrate, similarly to what was calculated for oxygen adlayers on the Ru(0001) surface.<sup>17</sup> Indeed, our calculations show a significant increase (1.4 eV) of the work function for Fe-silicate compared to that of the pristine silica adlayer.

In the next step, we address the experimentally observed phase separation into the Fe-containing and pure silica films. To investigate whether iron tends to segregate or prefers to be uniformly distributed in the film, total slab energies were calculated to estimate energies for the following reactions:



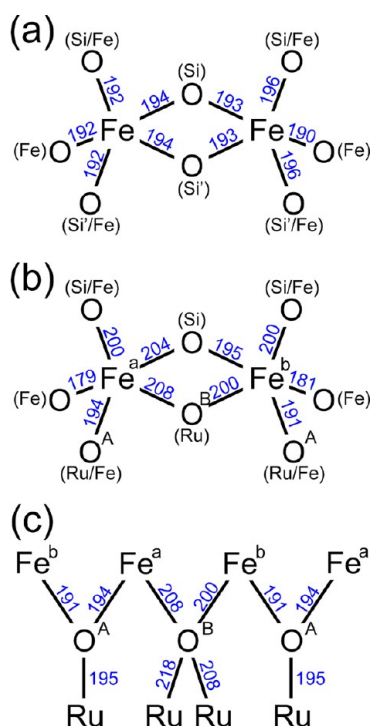


**Figure 7.** Schematic representation (cross view) of the iron coordination in two selected  $[\text{FeO}_5]$  square pyramids in (a) dehydroxylated nontronite<sup>15</sup> and (b)  $\text{Fe}_4\text{Si}_4\text{O}_{16}\cdot 2\text{O}/\text{Ru}(0001)$ , and (c) oxygen coordination in bridging Fe–O–Ru bonds in  $\text{Fe}_4\text{Si}_4\text{O}_{16}\cdot 2\text{O}/\text{Ru}(0001)$ . In parentheses: additional coordination partners (the prime indicates Si of the bottom silicate layer). A, B, a, and b differentiate between crystallographically inequivalent oxygen and iron atoms. Bond distances are in picometers.

Reaction 2 describes the disproportionation of two identical slabs, with one Fe atom in the unit cell, into one slab containing two Fe atoms and a pure silica slab. Reactions 3 and 4 are designed in a similar way, where the reaction coefficients account for the amount of iron in the system. The considerable energy gain observed for reaction 4 suggests that, indeed, the Fe atoms prefer to segregate into the Fe-rich structure, where all Si atoms in the bottom layer in the unit cell are substituted by Fe (see the model in Figure 5e). Therefore, the phase separation is thermodynamically driven, and the DFT results explain why the films at low Fe/Si ratios already show the structural and spectral characteristics of a fully covered Fe-silicate film.

**3.3. Discussion.** The above-presented experimental and DFT results provide compelling evidence that the Fe-silicate film grown on Ru(0001) should be described as a silica monolayer on top of an iron oxide monolayer over Ru(0001) with an  $\text{Fe}_4\text{Si}_4\text{O}_{16}$  composition. The simulated IRA spectrum nicely agrees with the experimental one, both showing a strong band at  $\sim 1005\text{ cm}^{-1}$  assigned to the Si–O stretching vibrations. Although the structure may contain oxygen atoms bound only to the Ru surface, their role seems to be marginal for the principal structure of the film. At lower Fe/Si ratios, iron atoms segregate, ultimately forming an Fe-silicate and pure silicate phases. As shown by DFT, this process is thermodynamically driven and seems to readily occur at high temperatures ( $\sim 1150\text{ K}$ ) necessary for the preparation of well-ordered films.

The Fe-silicate films are structurally very different from the similarly prepared aluminosilicate films, where Al is rather

uniformly distributed in the bilayer silicate framework,<sup>3</sup> basically following the Lowenstein rule<sup>6</sup> stating that Al–O–Al linkages are forbidden. In addition, in the aluminosilicate films, the charge imbalance for  $\text{Al}^{3+}$  present in the top layer is compensated by protons forming bridging (Si–OH–Al) hydroxyls clearly identified by IRAS.<sup>3</sup> In contrast, water adsorption experiments on the Fe-silicate films did not result in OH species, as judged by IRAS, that is in full agreement with the proposed structure exposing only hydrophobic siloxane O–Si–O species. The difference between the structural motifs in Al- and Fe-silicate films mimics the different behavior of naturally occurring Al- and Fe-silicate materials. In aluminosilicate films,  $\text{Al}^{3+}$  is present in four-fold coordination typical of natural zeolites (iron zeolites are not found in nature), whereas the Fe-silicate film adapts the layered structure of iron oxide–silica materials, characteristic for clay minerals.

It is instructive here to compare the atomic structures of the Fe-silicate film and of the natural mineral nontronite, representative of the Fe-rich smectites. An ideal nontronite is formed by two tetrahedral silicate sheets that sandwich an octahedral Fe-hydroxide sheet, thus classified as 2:1 to differentiate from 1:1 clay minerals formed by alternating tetra- and octahedral sheets. Since the film preparation involves water-free, oxygen atmosphere at high temperatures, we address the atomic structure of dehydroxylated nontronite,<sup>15</sup> depicted in Figure Sf (bottom). There is a clear similarity between these two, of the film and of the mineral, structures. The respective silica layers are virtually identical. Also the iron oxide layers are similar for both structures, although the order of connections between  $[\text{FeO}_5]$  square pyramids is slightly different. Another similarity is that the six-membered rings of the Si- and of the Fe-containing layers are not aligned and slightly shifted with respect to each other. In essence, the Fe-silicate film can be viewed as a single sheet of nontronite, where the third (silica) layer in the 2:1 sandwich is replaced by a metal support.

The coordination of iron atoms in both structures in the cross view is schematically shown in Figure 7. Fe–O distances in dehydroxylated nontronite fall in the narrow range of 190–196 pm,<sup>15</sup> whereas the bond lengths computed for the film are more scattered (i.e., from 179 to 208 pm). Such spread of values is indicative for considerable tension in the network. It should be mentioned, however, that the experimentally observed film rotation with respect to Ru(0001), not yet included in the calculations, may affect the interatomic distances to a certain extent.

The unit cell composition of dehydroxylated nontronite is  $\text{Si}_4\text{Fe}_2\text{O}_{11}$ , which can be written as  $(\text{Fe}_2\text{O}_3)(\text{SiO}_2)_4$  and implies an oxidation state of iron +III. Accordingly, the composition of the Fe-silicate film can be written as  $(\text{FeO}_2)_4(\text{SiO}_2)_4\cdot 2\text{O}/\text{Ru}(0001)$ , with an iron oxidation state +IV in the  $(\text{FeO}_2)_4(\text{SiO}_2)_4$  adlayer. However, since the metal surface is oxidized by the Fe-silicate, the adlayer is formally reduced, which implies a lower oxidation state of iron. Depending on the magnitude of charge transfer, one of the possibilities is one negative charge per  $\text{FeO}_2$  formula unit and hence an iron oxidation state +III, that is, the same as in nontronite. This would also be consistent with the formation of one bridging Fe–O–Ru bond per Fe atom between the Fe-silicate film and the Ru substrate. Experimental verification of the oxidation state of Fe in the films by XPS is not trivial, as the Fe 2p spectra show substantial final state effects<sup>18</sup> and therefore need further investigations in combination with state-of-the-art theoretical simulations.



## 4. CONCLUSIONS

Structural characterization, performed by a number of surface-sensitive techniques such as LEED, IRAS, XPS, and STM, in combination with DFT calculations, allowed us to determine the atomic structure of a well-ordered, ultrathin Fe-silicate film on a Ru(0001) substrate. The film can be considered as a monolayer of silica on top of a negatively charged iron oxide monolayer or as a sheet of a dehydroxylated nontronite, representative of Fe-rich smectites, with  $(\text{FeO}_2^-)_4(\text{SiO}_2)_4$  instead of  $(\text{Fe}_2\text{O}_3)(\text{SiO}_2)_4$  composition. The prerequisite for having a negatively charged layer is the presence of the supporting metal, which serves as an electron reservoir.

The results clearly highlight the differences between the principal structures of the Fe-silicate and previously studied aluminosilicate films, which reflect the known differences between naturally occurring materials.

In general, the results provide further information for rational preparation of model systems for a wide class of clay minerals and zeolite-like materials in the form of metal-supported thin films, well-suited for studying the surface chemistry of such complex materials.

## AUTHOR INFORMATION

### Corresponding Authors

Phone: +49 30 20937135. E-mail: js@chemie.hu-berlin.de.

Phone: +49 30 84134114. E-mail: shaikhutdinov@fhi-berlin.mpg.de.

### Author Contributions

<sup>§</sup>R.W. and X.Y. contributed equally.

### Notes

The authors declare no competing financial interest.

## ACKNOWLEDGMENTS

This article is dedicated to Rudolf Zahradník, Prague, on the occasion of his 85th birthday on October 20, 2013. This work has been supported by the German Science Foundation (DFG), by a computer grant from the North German Computing Alliance Berlin–Hannover (HLRN), and by the Funds of the Chemical Industry. J.A.B. thanks the Alexander von Humboldt Foundation for a fellowship. X.Y. acknowledges the International Max-Planck Research School “Complex surfaces in materials science”.

## REFERENCES

- (1) (a) Shaikhutdinov, S.; Freund, H.-J. *Adv. Mater.* **2013**, *25*, 49–67. (b) Shaikhutdinov, S.; Freund, H.-J. *ChemPhysChem* **2013**, *14*, 71–77.
- (2) (a) Yang, B.; Kaden, W. E.; Yu, X.; Boscoboinik, J. A.; Martynova, Y.; Lichtenstein, L.; Heyde, M.; Sterrer, M.; Włodarczyk, R.; Sierka, M.; Sauer, J.; Shaikhutdinov, S.; Freund, H.-J. *Phys. Chem. Chem. Phys.* **2012**, *14*, 11344–11351. (b) Loeffler, D.; Uhlrich, J. J.; Baron, M.; Yang, B.; Yu, X.; Lichtenstein, L.; Heinke, L.; Buechner, C.; Heyde, M.; Shaikhutdinov, S.; Freund, H.-J.; Włodarczyk, R.; Sierka, M.; Sauer, J. *Phys. Rev. Lett.* **2010**, *105*, 146104. (c) Yu, X.; Yang, B.; Boscoboinik, J. A.; Shaikhutdinov, S.; Freund, H.-J. *Appl. Phys. Lett.* **2012**, *100*, 151608.
- (3) Boscoboinik, J. A.; Yu, X.; Yang, B.; Fischer, F. D.; Włodarczyk, R.; Sierka, M.; Shaikhutdinov, S.; Sauer, J.; Freund, H.-J. *Angew. Chem., Int. Ed.* **2012**, *51*, 6005–6008.
- (4) (a) Panov, G. I. *CATTECH* **2000**, *4*, 18–31. (b) Zecchina, A.; Rivallan, M.; Berlier, G.; Lamberti, C.; Ricchiardi, G. *Phys. Chem. Chem. Phys.* **2007**, *9*, 3483–3499.
- (5) (a) Anke, N.; Michael, S.; Thomas, B. H. *Redox Properties of Structural Fe in Smectite Clay Minerals. Aquatic Redox Chemistry*; American Chemical Society: Washington, DC, 2011; Vol. 1071, pp

361–379. (b) Alexandrov, V.; Neumann, A.; Scherer, M. M.; Rosso, K. M. *J. Phys. Chem. C* **2013**, *117*, 2032–2040.

(6) Loewenstein, W. *Am. Mineral.* **1954**, *39*, 92–96.

(7) Ketteler, G.; Ranke, W. *J. Phys. Chem. B* **2003**, *107*, 4320–4333.

(8) (a) Kresse, G.; Furthmüller, J. *Comput. Mater. Sci.* **1996**, *6*, 15–50. (b) Kresse, G.; Furthmüller, J. *Phys. Rev. B* **1996**, *54*, 11169–11186.

(9) (a) Perdew, J. P.; Burke, K.; Ernzerhof, M. *Phys. Rev. Lett.* **1996**, *77*, 3865–3868. (b) Perdew, J. P.; Burke, K.; Ernzerhof, M. *Phys. Rev. Lett.* **1997**, *78*, 1396–1396.

(10) (a) Blöchl, P. E. *Phys. Rev. B* **1994**, *50*, 17953–17979.

(b) Kresse, G.; Joubert, D. *Phys. Rev. B* **1999**, *59*, 1758–1775.

(11) (a) Grimme, S. *J. Comput. Chem.* **2006**, *27*, 1787–1799.

(b) Kerber, T.; Sierka, M.; Sauer, J. *J. Comput. Chem.* **2008**, *29*, 2088–2097.

(12) Monkhorst, H. J.; Pack, J. D. *Phys. Rev. B* **1976**, *13*, 5188–5192.

(13) Boscoboinik, J. A.; Yu, X.; Yang, B.; Shaikhutdinov, S.; Freund, H.-J. *Microporous Mesoporous Mater.* **2013**, *165*, 158–162.

(14) Włodarczyk, R.; Sierka, M.; Sauer, J.; Löffler, D.; Uhlrich, J. J.; Yu, X.; Yang, B.; Groot, I. M. N.; Shaikhutdinov, S.; Freund, H.-J. *Phys. Rev. B* **2012**, *85*, 085403.

(15) Dainyak, L. G.; Zviagina, B. B.; Rusakov, V. S.; Drits, V. A. *Eur. J. Mineral.* **2006**, *18*, 753–764.

(16) Lindroos, M.; Pfnür, H.; Held, G.; Menzel, D. *Surf. Sci.* **1989**, *222*, 451.

(17) Stampfl, C.; Scheffler, M. *Phys. Rev. B* **1996**, *54*, 2868.

(18) (a) Bagus, P. S.; Ilton, E. S.; Nelin, C. J. *Surf. Sci. Rep.* **2013**, *68*, 273–304. (b) Schedel-Niedrig, T.; Weiss, W.; Schlögl, R. *Phys. Rev. B* **1995**, *52*, 17449–17460. (c) Yamashita, T.; Hayes, P. *Appl. Surf. Sci.* **2008**, *254*, 2441–2449.